

See discussions, stats, and author profiles for this publication at: <https://www.researchgate.net/publication/258261174>

# The physical mechanisms of step emulsification

Article in *Journal of Physics D Applied Physics* · February 2013

DOI: 10.1088/0022-3727/46/11/114003

---

CITATIONS

81

---

READS

540

4 authors, including:



Rémi Dangla

Stilla Technologies

16 PUBLICATIONS 1,523 CITATIONS

[SEE PROFILE](#)



Charles N Baroud

École Polytechnique

144 PUBLICATIONS 4,223 CITATIONS

[SEE PROFILE](#)

## The physical mechanisms of step emulsification

This article has been downloaded from IOPscience. Please scroll down to see the full text article.

2013 J. Phys. D: Appl. Phys. 46 114003

(<http://iopscience.iop.org/0022-3727/46/11/114003>)

View [the table of contents for this issue](#), or go to the [journal homepage](#) for more

Download details:

IP Address: 129.104.29.1

The article was downloaded on 28/02/2013 at 13:02

Please note that [terms and conditions apply](#).

# The physical mechanisms of step emulsification

Rémi Dangla<sup>1</sup>, Etienne Fradet<sup>1</sup>, Yonatan Lopez and Charles N Baroud

Ladhyx and Department of Mechanics, Ecole Polytechnique, CNRS, 91128 Palaiseau, France

E-mail: [baroud@ladhyx.polytechnique.fr](mailto:baroud@ladhyx.polytechnique.fr)

Received 2 August 2012, in final form 21 November 2012

Published 22 February 2013

Online at [stacks.iop.org/JPhysD/46/114003](http://stacks.iop.org/JPhysD/46/114003)

## Abstract

We revisit the physical balance that takes place when an interface between two immiscible fluids reaches a step change in the height of a microchannel. This situation leads to the production of droplets in a process known as ‘step emulsification’. However, the mechanism that is responsible for the drop breakup and that determines its size has not been explained in simple terms. We propose a geometric model for drop breakup based on a quasi-static balance between the curvature of the thread inside the inlet channel and the curvature of the “bulb” downstream of the step. We find that the confinement limits the lowest values of curvature that can be adopted by the thread. In contrast, the bulb curvature decreases as its size increases, which leads to a critical bulb radius beyond which the two regions cannot be in static equilibrium. This leads to a flow which breaks the bulb into a droplet. The critical bulb radius predicted by the geometric analysis is in good agreement with experimental measurements for different step and inlet channel geometries. The radius of the drop that detaches is therefore bounded from below by this value and increases slowly with the dispersed phase flow rate.

(Some figures may appear in colour only in the online journal)

## 1. Introduction

The production of drops and bubbles in microfluidic devices is a well studied and widely applied problem. In this context, a few standards have emerged and gained widespread acceptance, such as T-junctions or flow-focusing junctions [1–3]. In parallel to these widespread techniques, a few other methods have also appeared. Of these, step emulsification stands out for its simplicity and robustness. In this method, the microfluidic device is initially filled with the fluid that will form the outer phase. The dispersed phase fluid is then pushed into a microchannel that leads to a step change in height. Monodisperse drops are produced at this location and transported by the flow of the outer fluid.

Such devices were developed as microfabricated equivalents of membrane emulsification systems in order to take advantage of the advances in microfabrication technologies [4]. Since then, a series of papers (e.g. [5]) have shown that this technique is widely applicable and robust and that it can be used to produce monodisperse drops over a wide range of sizes, dictated mainly by the microchannel

depth. More recently, different groups have used steps in their microchannel designs in order to produce drops of a well calibrated size [6, 7], usually combining them with the classical T-junction or flow focusing junction.

Although the step emulsification technique has attracted widespread interest, there is no simple analytical expression to predict the size of drops that are produced by this technique. Instead, some phenomenological models have been suggested based on experimental measurements [8, 9]. In other cases, the dynamics of the interface has been modelled but solving these models generally requires heavy numerical solutions [5, 10–12]. A simple description for the physical mechanism that leads to the droplet detachment is still lacking.

Here we approach the problem of step emulsification from a geometric point of view, by studying the equilibrium shapes of the interface as it advances over the step in the microchannel. In a quasi-static situation, the curvature must be equilibrated everywhere in the system for the Laplace pressure jumps to be balanced. In particular, the curvature upstream of the step must adjust to the geometry of the interface downstream of the step, which is less confined and whose curvature decreases as its size grows. Yet, the strong confinement upstream of the step fixes a minimum value of the mean curvature ( $\kappa^*$ ) of

<sup>1</sup> These authors contributed equally to this work.

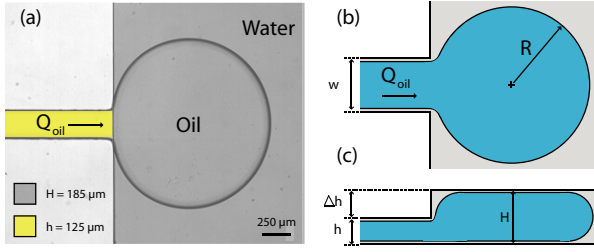


**Figure 1.** Problem geometry. (a) Top-down view: a bulb of oil injected into a water-filled reservoir. The width of the injection is  $w = 250 \mu\text{m}$  and increases to  $W = 5 \text{ mm}$  at the step, while the height increases from  $h = 125 \mu\text{m}$  to  $H = h + \Delta h = 185 \mu\text{m}$  in this example. (b) Top view sketch of the model geometry. (c) Side view of the same situation.

the interface below which equilibrium shapes no longer exist. We show that the curvature downstream of the step can reach values below  $\kappa^*$  and that the system comes out of equilibrium at this stage, leading to a drop breaking off over the step.

This droplet formation mechanism is generic to microchannel geometries with confinement asymmetries. It is detailed in section 2, where we relate the curvature criterion for the existence of equilibrium shapes to the volume of fluid downstream of the step. This yields an expression for the value of the drop radius  $R^*$  which triggers the collapse of the interface. This prediction is then tested experimentally, as explained in sections 3 and 4. Finally, these results are discussed in the context of microfluidics using confinement asymmetries in section 5.

## 2. A quasi-static mechanism for droplet formation

In order to address the droplet formation mechanism analytically, we consider the simplest microchannel geometry for droplet production at a step change in the channel height. It consists of a rectangular inlet channel of width  $w$  and height  $h$  ( $w > h$ ) that leads to a wide reservoir of increased height  $H = h + \Delta h$  filled with a quiescent fluid, as sketched in figure 1. Hence, the step is located at the junction between the inlet and the reservoir, in contrast with the original geometry where the change in channel height occurs some distance downstream of the inlet channel [4].

During its operation, the device is first filled with the continuous phase prior to injecting the dispersed phase at a constant flow rate. The dispersed phase forms a continuous thread in the inlet channel. At the entrance of the reservoir, the lateral confinement is suddenly released and the thread expands into a bulb of in-plane radius  $R$ , which grows as more fluid is injected.

We assume that the dispersed phase does not wet the channel walls and that a thin film of the continuous phase is always present. In this case, the interface geometry must be tangent to the wall at the point of apparent contact. This also implies that some of the continuous phase always remains in the inlet channel, in the form of corner gutters [13].

Next, we assume in our model that gravitational effects are negligible. These effects can be quantified by the Bond number

$Bo = \Delta\rho g H^2 / \gamma$ , where  $\Delta\rho$  is the difference in density between the two fluids,  $g$  is the acceleration due to gravity,  $H$  is the largest height in the device and  $\gamma$  is the interfacial tension. For the channel geometries we consider below, the Bond number remains in the range  $10^{-2}$ – $10^{-1}$ , which implies that gravitational effects may lead to corrections that are below 10% of our model predictions.

Last, provided that the injection flow rate is low, it is reasonable to assume that the system evolves in a quasi-static manner, i.e. that the interface around the thread and the bulb is in an equilibrium state at each instant. In this case, the shape of the interface must be such that its mean curvature  $\kappa$  is constant over the entire interface, apart from the regions where it is pressed against a channel wall and forced to follow the wall geometry.

The mean curvature  $\kappa$  is a local quantity defined at every point on the interface as the sum of the curvatures of the surface along its two principal directions (see [14, 15] for a detailed introduction). The Young–Laplace equation locally relates  $\kappa$  to the difference between the inner and outer pressures  $p_i$  and  $p_o$ , respectively, via the interfacial tension  $\gamma$ :

$$\gamma\kappa = p_i - p_o. \quad (1)$$

Hence, the quasi-static assumption also implies constant pressures in both phases, or equivalently that flow-induced pressure variations are negligible compared with the Laplace pressure jump  $\gamma\kappa$ . Finally, the quasi-static assumption is equivalent to requiring a small capillary number  $Ca = \mu Q / \gamma H^2 \ll 1$ , where  $\mu$  is a typical fluid viscosity and  $Q$  is the injection flow rate of the dispersed phase. In practice, our experiments always verify this condition.

Under these assumptions, it is pertinent to ask whether there exists an equilibrium shape for a bulb of size  $R$  connected to the thread in the inlet channel. Below, we begin by studying the equilibrium shapes of the thread upstream of the step and of the bulb in the reservoir separately. Then, we consider the equilibrium of the entire system by searching for situations when the curvature of the thread can match the curvature of the bulb.

### 2.1. Shape and curvature of the thread

We model the dispersed phase in the inlet channel as a semi-infinite fluid thread. A possible equilibrium shape of the interface is shown in figure 2(a). It is obtained using Surface Evolver [16] by imposing the Laplace pressure jump  $\Delta p = 4\gamma/h$  at the interface, or equivalently by imposing the mean curvature of the thread  $\kappa_{th} = 4/h$ . The thread is a straight cylinder of cross-section flattened against all four channel walls. The interface only bends in the corners along circular arcs of radius  $r = \kappa_{th}^{-1}$ , leaving out corner gutters of the continuous phase.

Equilibrium shapes of higher curvature are obtained by reducing the size of the gutters and thereby the radius of curvature  $r$  of the curved interface. However, the curvature of the straight cylinder geometry cannot decrease below the critical value  $\kappa^* = 2/h$ . When  $\kappa_{th} = \kappa^*$ , the top and bottom gutters meet at mid-height in the channel as shown on figure 2(b). The side interface is no longer pressed against

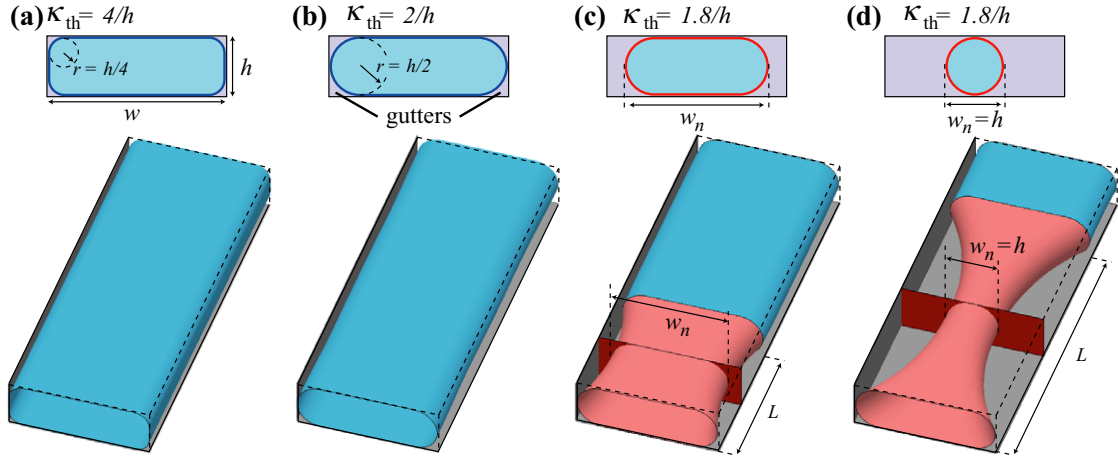


**Figure 2.** Shape of a confined thread in a rectangular channel (a) For a high curvature  $\kappa_{th} = 4/h$ , the thread is a straight cylinder of cross-section flattened against all four channel walls except near corners where the interface bends to form gutters. (b) When  $\kappa_{th} = 2/h$ , the gutters meet at mid-height in the channel and the lateral interfaces no longer flatten against the side walls. (c) Decreasing the imposed curvature to  $1.8/h$  leads to the necking of the thread. This shape is not in equilibrium and the necking region grows in time. (d) When the necking region becomes large enough, the thread becomes unstable locally by the Rayleigh–Plateau instability.

the lateral walls and has the shape of a semicircle of radius  $r = h/2$ . Given that the mean curvature  $\kappa_{th}$  of a straight cylinder is equal to the curvature of its cross-section, decreasing  $\kappa_{th}$  below  $2/h$  implies increasing  $r$  above  $h/2$ . This is impossible without violating the non-wetting boundary condition at the channel walls, which imposes that the interface intersects solid boundaries tangentially with a contact angle of  $\pi$ .

In fact, there are no equilibrium shapes of the interface if the imposed curvature is smaller than  $\kappa^* = 2/h$ . To illustrate this statement, we artificially impose  $\kappa_{th} = 1.8/h$  to a section of fixed length  $L$  of the thread while maintaining a curvature  $\kappa_{th} = 2/h$  over the rest of the interface using Surface Evolver. To reach the imposed curvature of  $1.8/h$ , the interface of the thread forms a neck as shown on figure 2(c). In this region, the thread maintains a transverse curvature of  $2/h$  in order to intersect the channel walls tangentially while bending inwards in the plane to feature a negative in-plane curvature of  $-0.2/h$ . However, although the shape of the neck locally reaches a stable geometry of constant mean curvature  $\kappa = 1.8/h$ , the thread is not at equilibrium globally since the curvature of the neck differs from the curvature of the rest of the thread. As we progressively extend the length  $L$  of the necking region, its width  $w_n$  decreases until it eventually matches the height of the channel  $h$ . In this configuration shown in figure 2(d), the centre of the neck detaches from all four channel walls and resembles an unconfined fluid thread which is prone to the Rayleigh–Plateau instability [17–19]. Increasing  $L$  any further triggers the collapse of the thread.

Overall, we find that a thread of non-wetting fluid confined in a rectangular channel is at equilibrium only when its curvature is higher than  $\kappa^* = 2/h$ . Otherwise, the thread is necessarily out of equilibrium, forms a neck, and then breaks in two.

## 2.2. Shape and curvature of the bulb

We now consider the equilibrium shape of the bulb in the reservoir which we model as a droplet of radius  $R$ , confined

between two solid plates separated by a distance  $H$ . Two limiting cases can be solved analytically.

- When the radius  $R$  of the drop is smaller than  $H/2$ , it takes a spherical shape since it is not confined. Its mean curvature is then  $\kappa_b = 2/R$ .
- The limit of a very large drop was studied by Laplace [20] and more recently by Park and Homsy [21]. The drop then has a pancake shape and a curvature

$$\kappa_b = \frac{2}{H} \left( 1 + \frac{\pi}{4} \frac{1}{\chi} \right), \quad (2)$$

where  $\chi = 2R/H \gg 1$  is the aspect ratio of the drop.

In all cases, the equilibrium shape of the interface away from the plates is an axisymmetric surface of constant mean curvature whose axis of symmetry is perpendicular to the plane of the reservoir. In the unbounded case, such surfaces are called Delaunay surfaces and can be classified into three subfamilies depending on the nature of their generatrix: catenoids, unduloids and nodoids [22]. Confinement only adds boundary conditions that dictate how the interface connects to the solid plates but it does not modify the generic differential equation  $\kappa = \text{cst}$  that generates the family of Delaunay surfaces. Consequently, the shape of a droplet confined between two parallel plates is a slice of a Delaunay surface.

In the case of a non-wetting droplet, the interface must intersect the plates tangentially with a contact angle  $\pi$ . This implies that at the walls, the tangent of the generatrix of the Delaunay surface is perpendicular to its axis of symmetry, a condition which is only met by nodoids. In a cylindrical coordinate system  $(\rho, \theta, z)$  centred at the centre of mass of the droplet, nodoids are described by the set of parametric equations

$$\rho(s) = \frac{\sqrt{e^2 - 1}}{\kappa_b} \sqrt{\frac{e - \cos s}{e + \cos s}} \quad (3a)$$

$$z(s) = \frac{e^2 - 1}{\kappa_b} \int_{\pi}^s \frac{-\cos u}{\sqrt{e^2 - \cos^2 u}(e + \cos u)} du. \quad (3b)$$

Here,  $e$  is a parameter that gives the nodoid shape and can vary from 1 to  $\infty$ ,  $s$  is a curvilinear coordinate, and  $u$  is an integration dummy variable.

The generatrix is  $2\pi$ -periodic in  $s$  and its tangent is perpendicular to the  $z$ -axis when  $dz/d\rho = 0$ , which occurs for  $s = \pi/2 + n \cdot \pi$ , with  $n$  an arbitrary integer. Intuitively, the interface of the squeezed drop must bend outwards and away from its axis of symmetry. This is the case for  $s = [\pi/2, 3\pi/2]$ . As a result, we obtain that the shape of a drop squeezed between two parallel plates is described by the set of parametric equations above with  $s$  varying between  $\pi/2$  and  $3\pi/2$ .

In equations (3a) and (3b), the curvature  $\kappa_b$  of the droplet is just a scaling factor. Hence, all possible geometries are scanned by varying  $e$  from 1 to  $\infty$ . For example, we recover the spherical shape when  $e \rightarrow 1$  while  $e \gg 1$  yields pancake droplets. In practice, for a given drop geometry or value of  $e$ ,  $\kappa_b$  is fixed by the height of the reservoir

$$H = \frac{e^2 - 1}{\kappa_b} \int_{\pi/2}^{3\pi/2} \frac{-\cos u}{\sqrt{e^2 - \cos^2 u}(e + \cos u)} du \quad (4)$$

and the radius  $R$  for the drop is obtained by taking  $s = \pi$  in equation (3a) for  $\rho(s)$ :

$$R = \frac{e + 1}{\kappa_b}. \quad (5)$$

Combining these expressions for  $R$  and  $H$ , we can express the mean curvature  $\kappa_b$  as a function of  $e$  and  $\chi$  in a compact equation

$$\kappa_b = \frac{2}{H} \frac{e + 1}{\chi}, \quad (6)$$

knowing that  $e$  is directly related to  $\chi$  via

$$\frac{1}{\chi} = \frac{e - 1}{2} \int_{\pi/2}^{3\pi/2} \frac{-\cos u}{\sqrt{e^2 - \cos^2 u}(e + \cos u)} du. \quad (7)$$

When the drop is spherical ( $e = 1$  and  $\chi = 1$ ), we recover  $H \cdot \kappa_b = 4$  as expected. In the asymptotic limit of large pancake drops ( $e \gg 1$ ),  $e = \chi + \pi/4 + \mathcal{O}(1)$  such that  $H \cdot \kappa_b = 2[1 + \pi/4\chi + \mathcal{O}(1/\chi)]$ , in agreement with the asymptotic limit (2) found by Laplace.

Overall, we can express  $H \cdot \kappa_b$  from the unconfined spherical case  $\chi < 1$  to the pancake droplet limit  $\chi \gg 1$  in the form  $H \cdot \kappa_b = 2[1 + f(\chi)]$ , with

$$\begin{aligned} f(\chi) &= \frac{2}{\chi} - 1 && \text{when } 0 < \chi < 1 \\ &= 1 && \text{for } \chi = 1 \\ &\approx \frac{\pi}{4} \frac{1}{\chi} && \text{when } \chi \gg 1 \end{aligned} \quad (8)$$

and find a lower bound  $2/H$  for the bulb curvature.

These results are shown in figure 3, where the different shapes are displayed along with the value of  $f(\chi)$ .

### 2.3. Matching curvatures: a scenario for droplet formation

The quasi-static equilibrium hypothesis implies that the mean curvature of the thread upstream of the step  $\kappa_{th}$  has to be equal

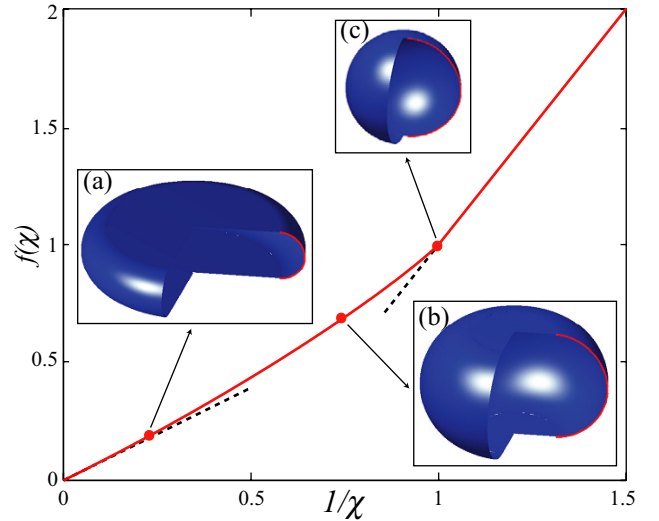


**Figure 3.** Plot of  $f = H \cdot \kappa_b/2 - 1$  versus the inverse aspect ratio of the bulb  $\chi$ . Insets (a)–(c) 3D plots of nodoid droplets obtained from the parametric equations (3a) and (3b) for (a)  $e = 3$ , (b)  $e = 1.5$  and (c)  $e = 1.001$ . The dashed lines represent the two analytical limits.

to the mean curvature of the bulb in the reservoir  $\kappa_b$ . Yet, we showed above that the mean curvature of the thread upstream of the step has a lower bound  $\kappa^* = 2/h$  below which it is out of equilibrium. By matching curvatures, this threshold curvature now also applies to the bulb. Consequently, the interface may evolve out of equilibrium and collapse to release a droplet in the reservoir when  $\kappa_b$  decreases below  $\kappa^* = 2/h$ .

The proposed scenario is the following: when the bulb first enters the reservoir, it is spherical. Its mean curvature is always higher than the critical value  $\kappa^*$  and the thread is strongly confined, as shown in figure 2(a). However, as more fluid is injected into the device, the size of the bulb increases while its mean curvature  $\kappa_b$  decreases. In the presence of a step, the lower bound  $2/H$  for the bulb curvature is lower than the critical curvature  $\kappa^* = 2/h$  of the thread. Hence, for any value of  $\Delta h > 0$ , the radius of the bulb eventually reaches a critical value  $R^*$  for which the curvature of the bulb is equal to  $\kappa^* = 2/h$ . The shape of the thread is then tangent to the channel side walls (figure 2(b)). Beyond this critical size  $R^*$ , the mean curvature of the thread can only match the bulb curvature by taking a negative value in the plane of the channel, as shown in figure 2(c). As discussed above, this situation is out of equilibrium. The pressure in the gutters around the thread is lower than the pressure in the reservoir. This drives a backflow of the continuous fluid, which in turn increases the size of the necking region. Eventually, the thread breaks when  $w_n = h$  and a drop of radius  $R^\infty$  detaches into the reservoir.

The critical radius  $R^*$  is defined by the equation  $\kappa_b = 2/h$ , which translates to

$$f(\chi^*) = \frac{\Delta h}{h} \quad (9)$$

for the critical aspect ratio  $\chi^*$  of the bulb. Recalling expression (8) and figure 3 for  $f(\chi)$ , we can solve this equation analytically for large step heights  $\Delta h/h > 1$  and numerically otherwise. When  $\Delta h/h > 1$ , we obtain that the



dispersed phase is out of equilibrium before the bulb becomes confined by the walls of the reservoir and the critical bulb size  $R^* = h$  is independent of the step height. As the step height  $\Delta h/h$  decreases,  $R^*$  increases, diverging along the asymptote  $R^* = \pi h H / 8 \Delta h$  when  $\Delta h/h \rightarrow 0$ . The full results are shown in section 4, figure 5.

### 3. Experimental methods

#### 3.1. Microchannel fabrication

The experiments were performed in PDMS microchannels (Dow Corning Sylgard 184). The microchannel fabrication was performed using dry film soft-lithography techniques [23], which allowed us to obtain different step heights by a successive lamination of different film types (Etertec, Eternal Laminar, thicknesses 15, 35, and 50  $\mu\text{m}$ )

The process began by (1) laminating the photoresist film layers onto a glass slide using an office laminator (PEAK PS320), at a constant temperature  $T = 100^\circ\text{C}$ , to get the base shape with the desired height. (2) The film was then exposed to UV light (Hamamatsu Lightningcure LC8) through a printed photomask corresponding to the inlet channel and the wide reservoir. (3) After exposing this channel, additional layers of film were added to obtain the desired height of the step. (4) The stack of photoresist films was exposed again to the UV light through a mask corresponding only to the reservoir region. (5) Finally the whole device was developed by immersing it in a solution of water at 1% (w/w) of carbonate potassium, to produce the master on which the PDMS could be moulded.

Once the moulds were fabricated, they were measured using an optical profilometer (Zygo). The measured values of the deconfinement parameter were in the range  $0.064 \leq \Delta h/h \leq 1.516$ , in addition to the condition of zero step height as a control. The height and width of the inlet channel were kept constant at  $h = 125 \mu\text{m}$  and  $w = 250 \mu\text{m}$ , except for the condition  $\Delta h/h = 0.064$  for which  $h = 250 \mu\text{m}$  and  $w = 500 \mu\text{m}$ . Once the moulds were measured, they were replicated into PDMS microchannels using the standard PDMS moulding techniques.

#### 3.2. Fluids and experimental protocol

The experiments were performed using a fluorinated oil (FC-40, viscosity  $\mu = 4 \text{ cP}$ ) as the dispersed phase. The continuous phase was a mixture of water and sodium dodecyl sulfate (SDS) at 3% concentration by weight. The interfacial tension  $\gamma$  was  $18 \text{ mN m}^{-1}$ . Good wetting of the water phase on the PDMS was ensured by using the channels within a few minutes after plasma bonding.

The channel was initially manually filled with the aqueous solution through specifically fabricated side holes, while ensuring that no gas bubbles were trapped. The oil was then injected using a programmable high precision syringe pump (Cetoni NeMESYS), at flow rates ranging from  $Q = 0.1$  to  $20 \mu\text{l min}^{-1}$  and each experiment was repeated three times. Images of the fluid exit through the channels were captured using a high-speed camera (Photron Fastcam 1024), mounted on a Nikon TE2000-U inverted microscope, filming at  $250 \text{ frames s}^{-1}$ .

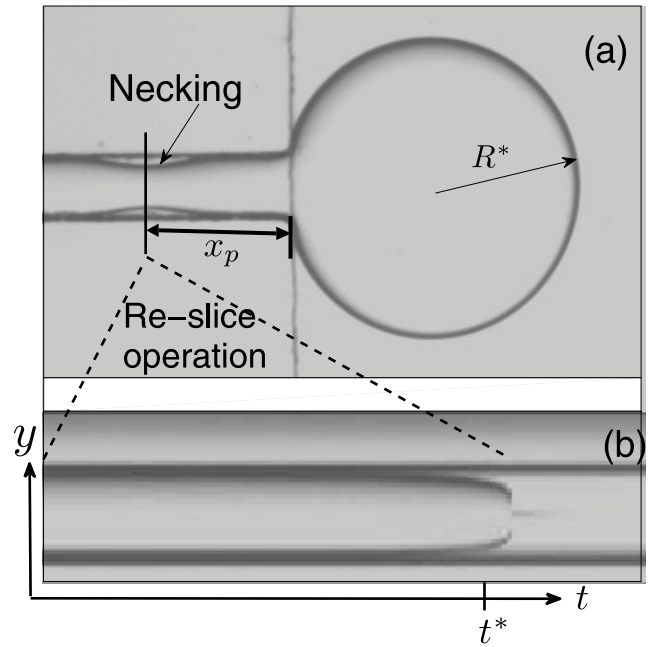


**Figure 4.** (a) The location of the neck formation is found from the late-time images of the drop detachment. (b) A space-time diagram is then constructed to determine the initial moments of the neck destabilization.

#### 3.3. Image analysis

Two radii were of interest in the movies that we captured: the final radius  $R^\infty$  was measured once the drop had detached. More importantly, we identified the radius  $R^*$  at which a neck began to form upstream of the step as shown in figure 4. This was done by first locating the position ( $x_p$ ) where the neck formed (figure 4(a)) and building space-time diagram of the grey values at this position (figure 4(b)). This allowed us to determine the time  $t^*$  at which the liquid interface began to separate from the walls; the bulb radius at this time was taken as the measure of  $R^*$ .

Note that the values of  $R^*$  that are reported here correspond to the smallest value of  $Q$ . Therefore, even though the criterion for stability depends on visually identifying the fluid detachment from the wall, the error on  $R^*$  is small since the drop volume changes very slowly.

### 4. Results

#### 4.1. Equilibrium loss

Using this experimental protocol, we first determined the value of the bulb radius at which the drop began to detach. The values of this critical radius  $R^*$  as a function of the step height  $\Delta h$  are shown in figure 5, where the physical values are normalized by the height  $h$  of the inlet channel. The experimental data (solid squares) were obtained for the minimum flow rate  $Q = 0.10 \mu\text{l min}^{-1}$  and the black solid line corresponds to the radius predicted by equation 9. This line is not a fit to the data as it does not contain any free parameters.

Both the model and the experiments show that the critical radius decreases with increasing deconfinement  $\Delta h/h$ . In fact,

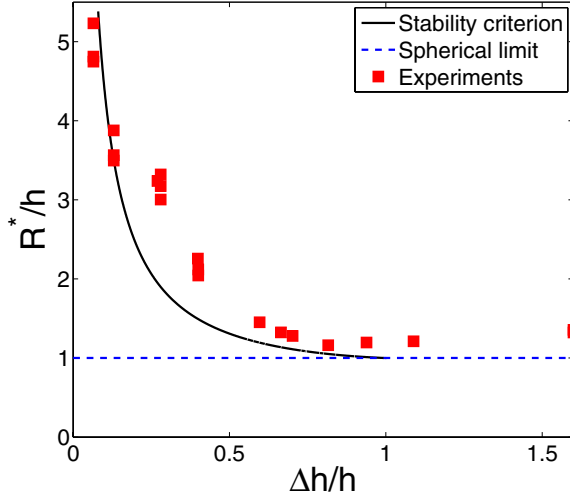


**Figure 5.** The evolution of  $R^*$  as a function of the step height. The points correspond to experimental measurements at a flow rate of  $Q = 0.01 \mu\text{l min}^{-1}$ . The solid line indicates the prediction from balancing the curvatures inside the inlet channel and in the deep section. The dashed line corresponds to the prediction for infinitely deep step.

the model predicts that the critical radius should diverge  $R^* \rightarrow \infty$  as  $\Delta h/h \rightarrow 0$ , which is in agreement with the experimental observations that yield  $R^* = 5h$  for  $\Delta h = 0.064h$ . Moreover, the control experiment with no step does not produce any drops, with the bulb remaining attached to the inlet channel. For  $\Delta h/h \geq 1$ , the model predicts that the critical radius should reach a plateau  $R^* = h$ . This plateau is observed in the experiments, although the measured critical radius is slightly superior to  $h$ .

The quantitative differences between the model and the measurements can be attributed to three main sources: first, gravitational effects can play a role, since FC-40 is about 85% denser than water. Second, the edge at which the inlet channel meets the reservoir may impose some corrections in order to account for the complex shape near the channel exit. Finally, slight variations in the photo-resist thickness can lead to a sloping top wall of the reservoir, which has been shown to significantly influence confined two-phase flows [24]. Nevertheless, the model and the experiments are in semi-quantitative agreement with no free adjustable parameters.

#### 4.2. Drop radius

In practical situations, the quantity of interest is the size of the final drop that detaches from the inlet channel. This drop radius ( $R^\infty$ ) corresponds to the critical value of the radius, augmented by the fluid in the thread downstream of the necking, which is small compared with the drop volume in our conditions. This must also be corrected for the further inflation of the drop by the fluid that has been injected during the necking time. If the necking time is independent of the flow rate, we would therefore expect the projected drop area to increase linearly with the flow rate to leading order, which would lead to the scaling  $(R^\infty - R^*) \sim Q^{1/2}$ . We expect that the necking time should decrease with increasing step height, since

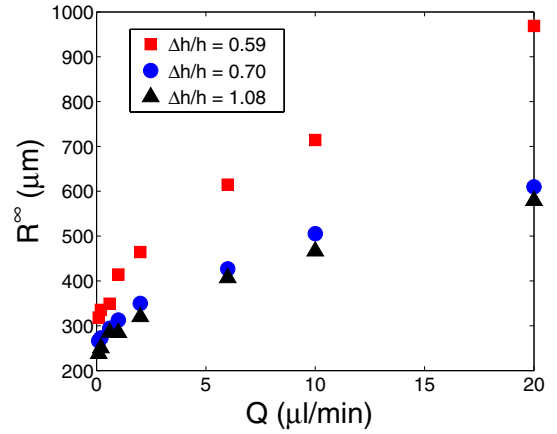


**Figure 6.** Final drop size ( $R^\infty$ ) as a function of the input flow rate ( $Q$ ) ranging between  $0.01$  and  $20 \mu\text{l min}^{-1}$ , for three representative step heights.

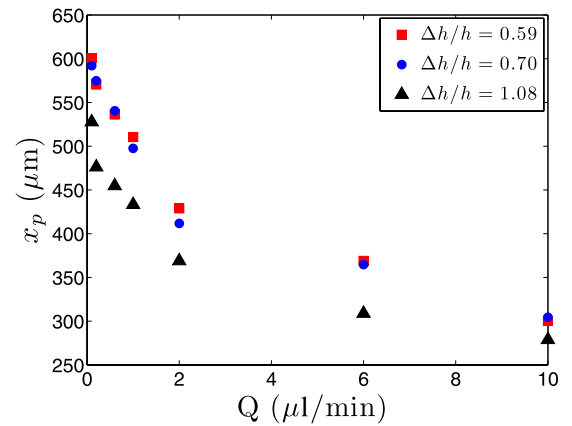


**Figure 7.** Position of the neck formation distance from the step as a function of the flow rate, for the same steps as figure 6.

the pressure imbalance that drives the necking of the thread increases with  $\Delta h$ .

We measured the drop radii ( $R^\infty$ ) as a function of the flow rate at which the dispersed phase is injected. As shown in figure 6, we observe that the drop size indeed increases with the flow rate, in agreement with the ‘inflationary’ theory. Nonetheless, the change in drop radius is small, since at most a three-fold difference in radius (9 times in volume) is observed for a two-thousand fold increase in flow rate ( $Q$  from  $0.01$  to  $20 \mu\text{l min}^{-1}$ ). A fit of  $R^\infty - R^*$  yields a power law of exponent larger than  $0.5$ , between  $0.6$  and  $0.7$ . This indicates that the necking time depends on the flow rate. Moreover, we find that the drop size decreases with increasing step height regardless of the oil flow rate. This implies that the variations in the necking time are not sufficient to modify the hierarchy of sizes dictated by the dependence of  $R^*$  on  $\Delta h$ .

#### 4.3. Breakup distance

Finally, it is worth noting the location of the necking which leads to the drop breakup  $x_p$ . This position depends on the flow rate of the inner phase, as shown in figure 7. In fact, the geometric mechanism presented here provides a prediction for the critical bulb radius but it cannot predict where the neck



will form. Predicting  $x_p$  would require a dynamic model that accounts for the back flow into the inlet channel and its interactions with the fluid thread. Such a model would need to take into account the fluid properties, as well as geometric details about the inlet channel.

## 5. Summary and discussions

In this paper, we present a theory for step emulsification based on quasi-static geometric arguments. We argue that the growth of the bulb in the reservoir leads to a thinning of the thread in the inlet channel in order to maintain a curvature equilibrium between the two regions. We also identify a minimum value of curvature, imposed by the confinement of the thread in the inlet channel, below which equilibrium shapes of the interface cannot exist. A geometric calculation then shows that the bulb curvature always decreases below this critical value if the reservoir has a larger height than the inlet channel. This forces the system out of equilibrium: a backflow of the continuous phase is generated upstream of the step, which leads to the drop breakup.

The curvature balance model does not depend on the fluid properties. In particular, it is insensitive to the value of the interfacial tension even though the physics that we describe is dominated by surface effects. This is because the interfacial tension is acting in both regions of the microchannels and its value drops out of the balance.

However, our model does not directly predict the actual size of the drops that are formed. Instead, we provide a lower bound for the drop size, which must then be corrected for dynamical effects. Those effects do depend on the fluid properties: the back flow that is driven into the inlet channel is accelerated by the capillary pressure imbalance (which depends on  $\gamma$ ) and slowed down by viscous effects (which depend on  $\mu$ ) and by the overpressure due to the driving (which depends on the flow rate  $Q$ ). In order to reduce the impact of the dynamics on the drop size, one may imagine designing the inlet channel with local modulations in width or depth in order to facilitate the breakup.

Finally, note that the curvature imbalance can also be produced by a more gradual change in the channel height. We have recently shown [24] that droplets with well calibrated sizes can be produced by a sloping channel, through a similar mechanism. In the case of a sloping roof, the drop size depends on the inlet channel geometry, as in the present case, but also on the slope angle. Moreover, the slope provides a mechanism to move the droplet after its formation, since the drops feel a force that drives them towards the regions of lowest confinement [25]. When combined with local modulations of the channel height [26, 27], such an approach can lead to a new generation of droplet microfluidics that does not require any flow of the continuous phase.

## Acknowledgments

The authors thank Caroline FROT for technical assistance on the project. The research leading to these results has received

funding from the European Research Council under the European Union's Seventh Framework Programme (FP7/2007-2013)/ERC Grant agreement no 278248 'MULTICELL'.

## References

- [1] Christopher G F and Anna S L 2007 Microfluidic methods for generating continuous droplet streams *J. Phys. D: Appl. Phys.* **40** R319–36
- [2] Baroud C N, Gallaire F and Dangla R 2010 Dynamics of microfluidic droplets *Lab Chip* **10** 2032–45
- [3] Seemann R, Brinkmann M, Pfohl T and Herminghaus S 2012 Droplet based microfluidics *Rep. Prog. Phys.* **75** 016601
- [4] Sugiura S, Nakajima M, Iwamoto S and Seki M 2001 Interfacial tension driven monodispersed droplet formation from microfabricated channel array *Langmuir* **17** 5562–6
- [5] Kobayashi I, Mukataka S and Nakajima M 2005 Novel asymmetric through-hole array microfabricated on a silicon plate for formulating monodisperse emulsions *Langmuir* **21** 7629–32
- [6] Priest C, Herminghaus S and Seemann R 2006 Generation of monodisperse gel emulsions in a microfluidic device *Appl. Phys. Lett.* **88** 024106
- [7] Malloggi F, Pannacci N, Attia R, Monti F, Mary P, Willaime H, Tabeling P, Cabane B and Poncet P 2010 Monodisperse colloids synthesized with nanofluidic technology *Langmuir* **26** 10–1441
- [8] Sugiura S, Nakajima M and Seki M 2002 Prediction of droplet diameter for microchannel emulsification *Langmuir* **18** 3854–9
- [9] Stoffel M, Wahl S, Lorenceau E, Höhler R, Mercier B and Angelescu D E 2012 Bubble production mechanism in a microfluidic foam generator *Phys. Rev. Lett.* **108** 198302
- [10] Christov N C, Danov K D, Danova D K and Kralchevsky P A 2008 The drop size in membrane emulsification determined from the balance of capillary and hydrodynamic forces *Langmuir* **24** 1397–410 PMID: 17963414
- [11] van Dijke K C, Schroën K C P G H and Boom R M 2008 Microchannel emulsification: From computational fluid dynamics to predictive analytical model *Langmuir* **24** 10107–15 PMID: 18702473
- [12] van der Zwan E, Schroën K and Boom R A 2009 geometric model for the dynamics of microchannel emulsification *Langmuir* **25** 7320–7
- [13] Wong H, Morris S and Radke C J 1992 Three-dimensional menisci in polygonal capillaries *J. Colloid Interface Sci.* **148** 317–36
- [14] Eggers J G and Villermaux E 2008 Physics of liquid jets *Rep. Prog. Phys.* **71** 036601
- [15] Ajaev V S and Homsy G M 2006 Modeling shapes and dynamics of confined bubbles *Ann. Rev. Fluid Mech.* **38** 277–307
- [16] Brakke K A 1992 The Surface Evolver *Exp. Math.* **1** 141–65
- [17] Garstecki P, Stone H A and Whitesides G M 2005 Mechanism for flow-rate controlled breakup in confined geometries: a route to monodisperse emulsions *Phys. Rev. Lett.* **94** 164501
- [18] Raven J P and Marmottant P 2009 Microfluidic crystals: dynamic interplay between rearrangement waves and flow *Phys. Rev. Lett.* **102** 084501
- [19] van Steijn V, Kleijn C R and Kreutzer M T 2009 Flows around confined bubbles and their importance in triggering pinch-off *Phys. Rev. Lett.* **103** 214501
- [20] Laplace P S 1806 *Traité de mécanique céleste; supplément au dixième livre, sur l'action capillaire*, Courcier, Paris
- [21] Park C W and Homsy G M 1984 Two-phase displacement in Hele Shaw cells: theory *J. Fluid Mech.* **139** 291–308

- [22] Delaunay C 1841 Sur la surface de revolution dont la courbure moyenne est constante *J. Math. Pures Appl.* **6** 309–15
- [23] Stephan K, Pittet P, Renaud L, Kleimann P, Morin P, Ouaini N and Ferrigno R 2007 Fast prototyping using a dry film photoresist: microfabrication of soft-lithography masters for microfluidic structures *J. Micromech. Microeng.* **17** N69–74
- [24] Dangla R, Kayi S C and Baroud C N 2013 Droplet microfluidics driven by gradients of confinement *Proc. Natl. Acad. Sci. USA* (in press) doi:[10.1073/pnas.1209136110](https://doi.org/10.1073/pnas.1209136110)
- [25] Dangla R, Lee S and Baroud C N 2011 Trapping microfluidic drops in wells of surface energy *Phys. Rev. Lett.* **107** 124501
- [26] Abbyad P, Dangla R, Alexandrou A and Baroud C N 2011 Rails and anchors: Guiding and trapping droplet microreactors in two dimensions *Lab Chip* **11** 813–21
- [27] Fradet E, McDougall C, Abbyad P, Dangla R, McGloin D and Baroud C N 2011 Combining rails and anchors with laser forcing for selective manipulation within 2D droplet arrays *Lab Chip* **11** 4228–34